Investigation of Failure Mechanism of Al₂O₃ Specimens Subjected to Three-Point Bending Test

Mikhail Eremin, Alexey Kulkov
Institute of Strength Physics and Materials Science of Siberian Branch of Russian Academy of Sciences, Russia
eremin@ispms.ru, http://orcid.org/0000-0002-5740-8221
727@ispms.ru, http://orcid.org/0000-0003-2345-6792

Igor Smolin, Valentina Mikushina
Institute of Strength Physics and Materials Science of Siberian Branch of Russian Academy of Sciences, Tomsk State University, Russia
smolin@ispms.ru, http://orcid.org/0000-0003-3167-9530
mikushina_93@mail.ru, http://orcid.org/0000-0001-6780-5717

ABSTRACT. Experimental loading and FEM simulation-based approach at macroscale are utilized to investigate the failure mechanisms of Al₂O₃ ceramics. Experimental characterization of the microstructure is carried out using SEM. Recently the mesoscale models of a representative volume of porous alumina ceramics were built on the basis of grain and pore distribution patterns and subjected to uniaxial loading in order to determine effective mechanical characteristics which are utilized for macroscopic simulation in this work. Pre-fracture behavior of specimens undergoes the Drucker-Prager model with non-associated plastic flow rule. Experimental and numerical simulation fracture patterns show that material exhibits predominantly mode I, sometimes passing to mixed mode I+II of crack propagation. Comparison of experimental data and numerical simulation data gives a good agreement.

KEYWORDS. Alumina ceramics; Three-point bending; Crack propagation; Fracture criterion; Experiment; Numerical simulation.

INTRODUCTION

One of the effective ways of obtaining porous alumina ceramics is slip casting with pore-producing dopants which burn out during the sintering [1]. Porous alumina ceramics are widely used as catalyst supports, filters, coatings, etc. [2]. Pore's size and morphology strongly affect the macroscopic failure behavior of devices on their basis, which maintains the research interest of these topics [3]. As well as many other ceramics on the basis of metal oxides,

alumina ceramics possess brittleness which decreases significantly the operational functionality of devices. This is due to a decrease of elastic and strength characteristics of materials with an increase of porosity.

The multiscale modeling approach has been recently successfully applied for investigation of failure mechanisms of different materials [4]. It appears to be useful since it provides a bridge between the microstructure of the material and effective mechanical characteristics utilized for macroscopic simulation.

Recently [5] the mesoscale models of a representative volume of porous alumina ceramics were built on the basis of grain and pore distribution patterns and subjected to uniaxial loading in order to determine effective mechanical characteristics which are utilized for macroscopic simulation in this work.

In the next sections, we provide a microstructural analysis of sintered specimens using scanning electron microscopy. We provide a mathematical statement of the boundary value problem (BVP). FEM simulation-based approach is utilized to investigate the failure mechanisms of Al_2O_3 ceramic specimens subjected to three-point bending. We also performed a comprehensive numerical analysis of the failure mechanism. The results of a macroscopic simulation are compared with experimental data and give a good agreement in terms of loading diagram and crack path.
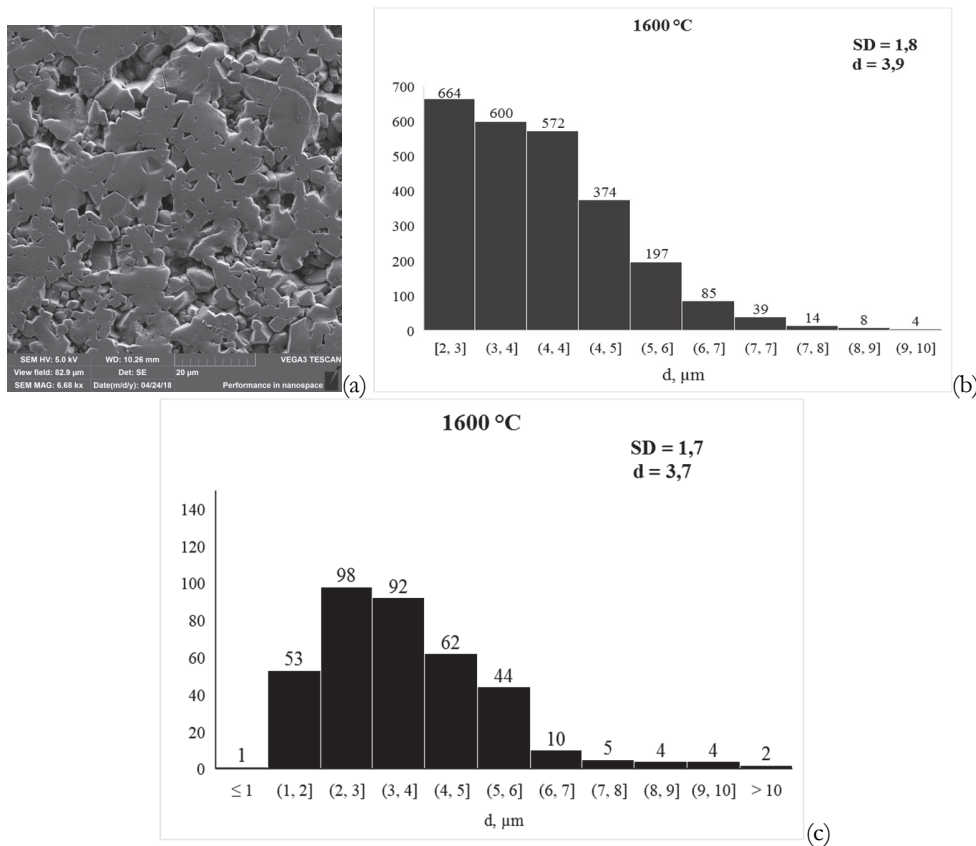

Figure 1: Fracture surface of Al_2O_3 sample after etching, sintered at 1600° C (a), the pore size (b) and the grain size distributions (c) of the ceramic specimen. Images obtained using a scanning electron microscope in SE mode (SD means standard deviation, d stands for average dimension).

MATERIAL CHARACTERIZATION AND EXPERIMENTAL SETUP

Rectangular shaped specimens of Al_2O_3 were obtained from technically pure alumina powder by slip casting and sintering, the rate of temperature increase was 3.5°C/min and the specimens were kept at the temperature of 1600°C in a conventional oven during one hour. A detailed study of the microstructure of the samples was carried out. Analysis of the structure allowed us to identify the morphological features of the pore space and the size of structural elements such as grains and pores. Porosity was determined by ImageJ software [2] from photos obtained with the help of SEM Vega 3 LMU. Photos of the etched surface of the samples are presented in Fig. 1a. The average porosity of the samples is 17%. The average pore size is 3.9 microns (Fig. 1b). The pore size varies from 1 to 8 microns, and the maximum is

observed from 2 to 3 microns. The grain size distribution chart shows that the bulk of the grains are between 1 and 6 microns (Fig. 1c).

Three-point bending of specimens was carried out using universal loading machine Instron 1185 in the deformation-controlled mode with the rate of 0.1 mm/min (Fig. 2). We tested a total of 6 specimens. Fig. 3a illustrates the experimental diagrams as received after testing. Experiments show that the scatter of loading diagrams is quite large. The average tensile strength in three-point bending experiments was about 270 MPa. The average Young's modulus was 115.5 GPa. The initial stages of loading are associated with the adjustment of the specimens and, probably, some internal non-linear mechanisms, this part of the diagram has a non-linear backward deflection and its physical meaning is poorly understood in the case of three-point bending. Experimental diagrams for specimens 1, 9, 10, 11 are in good agreement, scatter of slopes is in the satisfactory range of approximately 15%. However, specimens 7 and 12 have lower slopes of the tangential line at elastic stage approximately 1.3-1.5 times lower than for other specimens. Physically, such lower slopes can be explained by the existence of large pores and also by more insufficient quality of specimens after sintering. Fig. 3b represents experimental fracture patterns of specimens.
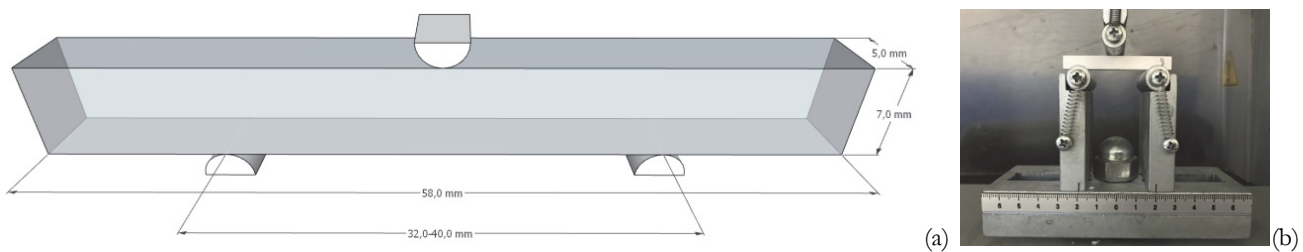

Figure 2: Schematic representation of the loading scheme and dimensions of a specimen (computational domain) (a), real experimental setup (b).
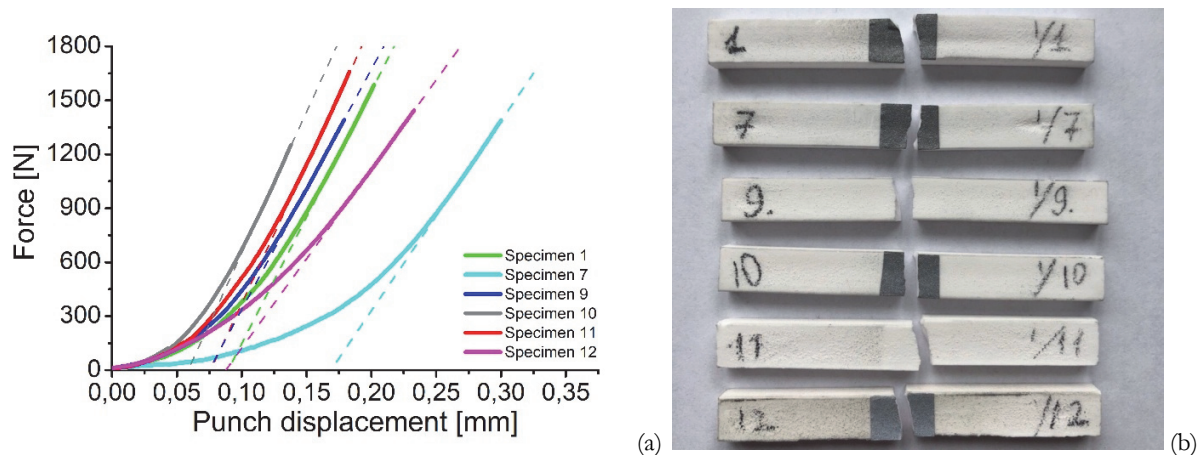

Figure 3: Experimental loading diagrams as received, dashed lines illustrate the slope of a linear elastic stage of the specimen's deformation (a), fractured specimens (b).

THE MATHEMATICAL STATEMENT OF THE PROBLEM

The FEM simulation-based approach is utilized in this work with linear tetrahedron elements [6]. It is a compulsory assumption for the needs of current work since the material experiences small strains.

The core of FEM is represented by the fundamental laws of mass and momentum conservation. The system of equations is completed by the formulation of corresponding constitutive equations for elastic and inelastic behavior. Thus, for elastic behavior, we use constitutive equations of hypo-elastic media (Eqn. 1) and Drucker-Prager (DP) yield criterion [7] (Eqn. 2) with non-associated plastic flow rule for inelastic behavior.

$$\dot{P} = -K(\dot{\theta}^T - \dot{\theta}^P) , \dot{S}_{ij} = 2\mu\left(\dot{\varepsilon}_{ij}^T - \dot{\varepsilon}_{ij}^P - \frac{1}{3}\left(\dot{\theta}^T - \dot{\theta}^P\right)\delta_{ij}\right), \dot{\theta}^T = \dot{\varepsilon}_{ii}^T , \dot{\theta}^P = \dot{\varepsilon}_{ii}^P , 2\dot{\varepsilon}_{ij}^T = v_{i,j} + v_{j,i} \qquad (1)$$

where P is hydrostatic pressure, S_{ij} are components of the deviatoric stress tensor, K is bulk modulus, μ is shear modulus, $\dot{\theta}^T$ is volumetric total strain rate, $\dot{\theta}^P$ is volumetric inelastic strain rate, ε_{ij}^T are components of total strain tensor, ε_{ij}^P are components of inelastic strain tensor, v_i are velocity vector components, dot over the symbols means a time derivative.

$$f\left(\sigma_{ij}\right) = -\alpha P + \tau - Y = 0 , \tau = \sqrt{\frac{1}{2}S_{ij}S_{ij}} \qquad (2)$$

where $f\left(\sigma_{ij}\right)$ is an equation of yield surface, τ is the second invariant of the deviatoric stress tensor, α and Y are two material constants within DP model which provide links to material cohesion and internal friction angle [7].
Equation of plastic potential is given by (Eqn. 3):

$$g(\sigma_{ij}) = \tau - \Lambda P + const \qquad (3)$$

where Λ is a dilatancy factor. Utilizing the main equation of the theory of plasticity and multiplying all parts of the equation on time step of integration dt, we obtain the equation for inelastic strain tensor components increments (Eqn. 4):

$$d\varepsilon_{ij}^P = d\lambda\frac{\partial g}{\partial \sigma_{ij}} , d\varepsilon_{ij}^P = d\lambda\left[\frac{S_{ij}}{2\tau} + \frac{\Lambda}{3}\delta_{ij}\right] \qquad (4)$$

Once we derived the plastic potential equation and obtained the inelastic strain increments we inserted the procedure of stresses correction as an outer procedure to the existing FEM code. The procedure of correction is described below (Eqn. 5-6).

$$d\lambda = \frac{f^*(\sigma_{ij})}{K\alpha\Lambda + \mu} , d\varepsilon^P = \Lambda d\lambda , d\gamma^P = \sqrt{\frac{2}{3}de_{ij}^P de_{ij}^P} = \frac{d\lambda}{\sqrt{3}} \qquad (5)$$

$$P = P^* + Kd\varepsilon^P , \tau = \tau^* - \sqrt{3}\mu d\gamma^P \qquad (6)$$

where $d\lambda$ is a multiplier from the main equation of the theory of plasticity, symbol * is related to the unrelaxed stresses, $d\varepsilon^P$ is dilatancy increment, $d\gamma^P$ is an increment of the intensity of inelastic strains, de_{ij}^P are increments of deviatoric part of inelastic strains tensor components.
In order to describe the fracture process, we utilize a simple fracture criterion: when the accumulated intensity of inelastic strains γ^p exceeds a critical value γ_c in some element, then the material is assumed to be fractured in this point. After fracture occurs, the material behavior is described as follows: if the rate of total volumetric strain is positive then all components of stress tensor are nullified. Otherwise (total volumetric strain is negative) the procedure of stresses relaxation correction is carried according to the Eqn. 2-6.
Physical-mechanical properties of alumina ceramics are given in the Tab. 1. Strength and elastic parameters in the model are determined from mesoscale simulation [5] and validated on the basis of the experimental study through a large number of iterations. This term needs some explanation for our opinion. Generally, it is practically impossible to carry out the uniaxial loading experiments with specimens of mesoscopic scales, i.e. approximately 100-200 μm. Thus, we must first determine the properties of the material on the basis of experimental data on the loading of laboratory scale specimens, secondary, we carry out a macroscopic simulation and validate the model parameters and thirdly, we must solve the mesoscale BVP, so that the effective characteristics would correspond to macroscopic ones. Several top-to-bottom and bottom-to-top iterations

of the simulation are necessary to adjust the model parameters and obtain the convergence between meso and macro levels. The dilatancy factor Λ was chosen after the results of the numerical simulation which fit well the experimental results.

Material	ϱ [g/cm³]	K [GPa]	μ [GPa]	Y [MPa]	α	Λ	γ_C
Al₂O₃	2.697	97	64	220	0.65	0.1	0.001

Table 1: Physical-mechanical properties of alumina ceramics

Boundary conditions applied to the computational domain are formulated in terms of kinematic boundary conditions and correspond to the scheme given in Fig. 2. Punch displacement is simulated by assigning of nodal displacements under the contact, supports are simulated by the zero-vertical component of nodal displacements under the corresponding contact patches. Other displacements are not confined.

RESULTS OF NUMERICAL SIMULATION AND DISCUSSION

Three-point bending usually causes the propagation of mode I crack in the middle part of the specimen from the bottom edge to the zone of load application [8]. Obviously, the middle part of the specimen is the zone of high interest where the fracture process should be described as accurate as possible. The propagation of crack through the specimen cross-section necessitates the convergence test of numerical solution of BVP. We need to refine the mesh in the fracture process zone in order to achieve a stable solution when the increase of elements number will no longer have an effect on the value of maximum stress intensity. Fig. 4a illustrates the convergence analysis of numerical simulation results. We recorded the average intensity of stresses through the entire computational domain and increased the number of elements in the domain from approximately 380000 to 2000000. Simulation results show that the convergence of results occurs when the number of elements is greater than 1000000. For further investigation, we stopped on the fine mesh quality of approximately 2000000 elements. Model design and meshing were carried out using ANSYS software (Fig. 4b).
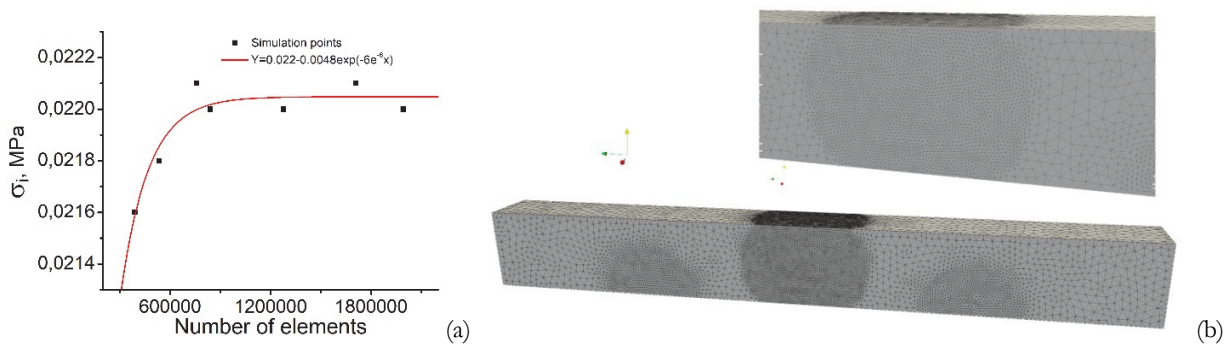

Figure 4: Convergence of the results of numerical simulation, σ_i is a maximum intensity of stress in the whole computational domain (a), mesh in the computational domain with ≈1200000 elements (b).

To identify the failure mechanisms of specimens at three-point bending, the dynamics of stress and strain state was traced. Fig. 5a shows the distribution of the stress tensor component σ_{zz}, acting along the largest dimension of the specimen. The concentration region of σ_{zz} is in the middle of the specimen, as well as near the supports (Fig. 5b). This suggests that even in the elastic stage of loading, conditions are created for the formation of a mode I crack under the action of normal stresses. Although this does not exclude the possibility of changing the crack propagation mode from mode I to a mixed type if the tangential stresses become significant.

Fig. 6a illustrates the comparison of the loading diagrams obtained in the experiment with the diagram obtained in numerical simulation. Calculations show that a sample based on alumina with a 17% pore content experiences brittle failure, which is also confirmed by an analysis of the nucleation and propagation of a crack. The origin of the crack occurs when the displacement of the nodes in the contact patch is approximately 0.04892 mm. Prior to this displacement material undergoes elastic deformation. The crack propagation, up to macrofracture, takes approximately another 0.0001 mm of nodal

displacement, which is about 0.2% of the total deformation (Fig. 6b). It proves that, generally, macroscopic behavior is brittle.
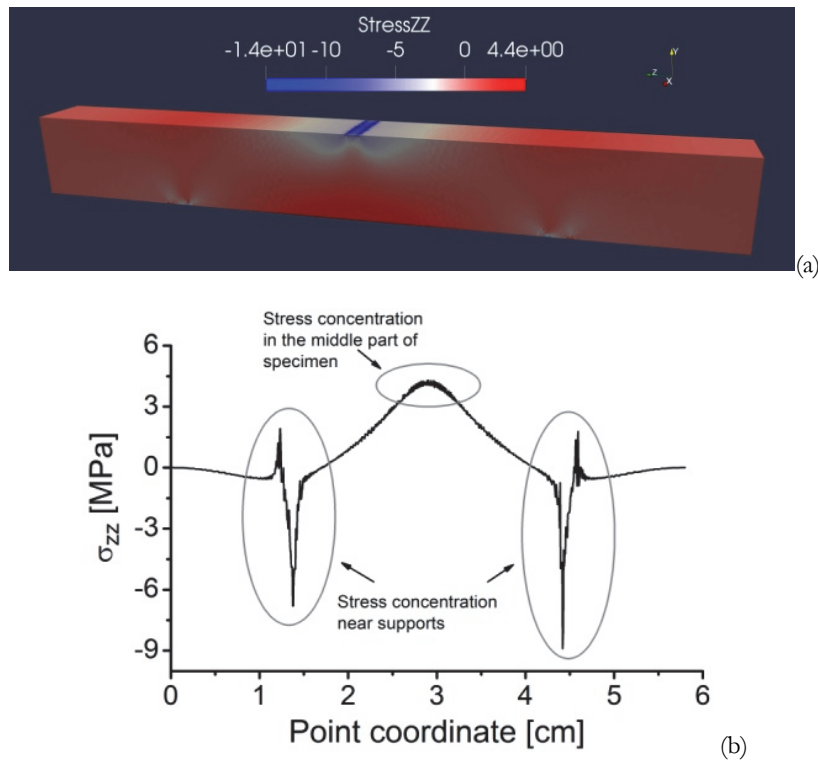

Figure 5: Pattern of σ_{zz} [MPa] stress in the elastic stage of loading (a), graphical representation of σ_{zz} stress distribution at the bottom edge of the specimen (b).
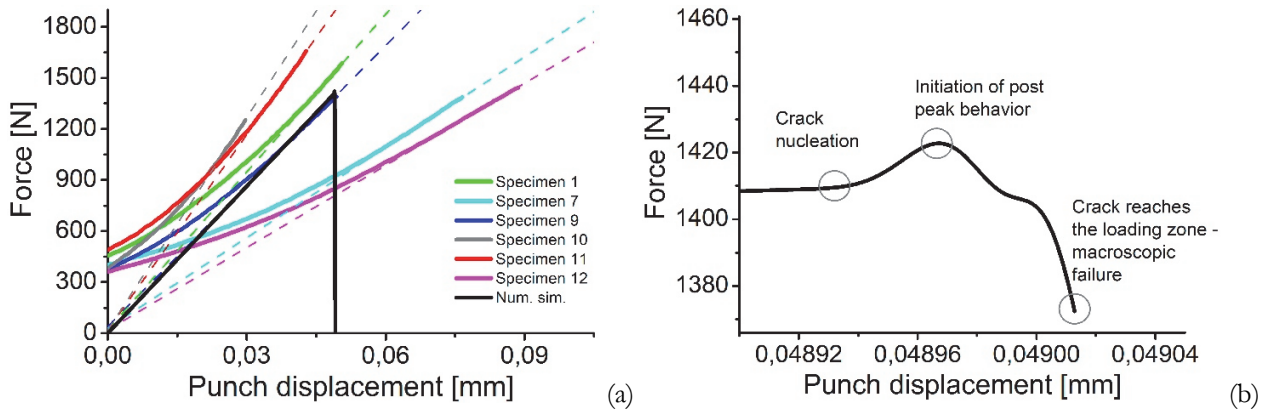

Figure 6: Comparison of numerical simulation diagram against the experimental loading diagrams (a), stages of failure related to loading diagram (b).

Slight prolongation of the fracture process is due to (i) crack branching, which is observed at initial stages of crack propagation in the lower part and (ii) crack bifurcation in the upper part of a bended cantilever. The tortuous crack path stands for the more effective energy dissipation than a single crack.

The crack branching, observed at the initial stage of deformation in the lower part of a bended cantilever, finally stops. Hence, the main fracture mechanism at this stage of deformation is namely Mode I.

When the crack tip meets the zone of compressive stresses, which is generally formed in the upper part of a bended cantilever, according to the loading history, the crack bifurcation occurs. The crack bifurcation is related to the rotation of the maximum principal stress axis (Fig. 7a, b). Fig. 7a illustrates the directions of the maximum principal stress axis at the

elastic stage of deformation prior to the crack formation. Fig. 7b illustrates the rotation of axis near the tips of crack after bifurcation.

Finally, both cracks deviate to the direction of load application zone and provide the macroscopic failure of the specimen. Stage of macroscopic fracture is illustrated in Fig. 7c with two magnified views of crack contour.

The final pattern of macroscopic fracture is illustrated in Fig. 8. Two views from opposite sides of the specimen are illustrated.
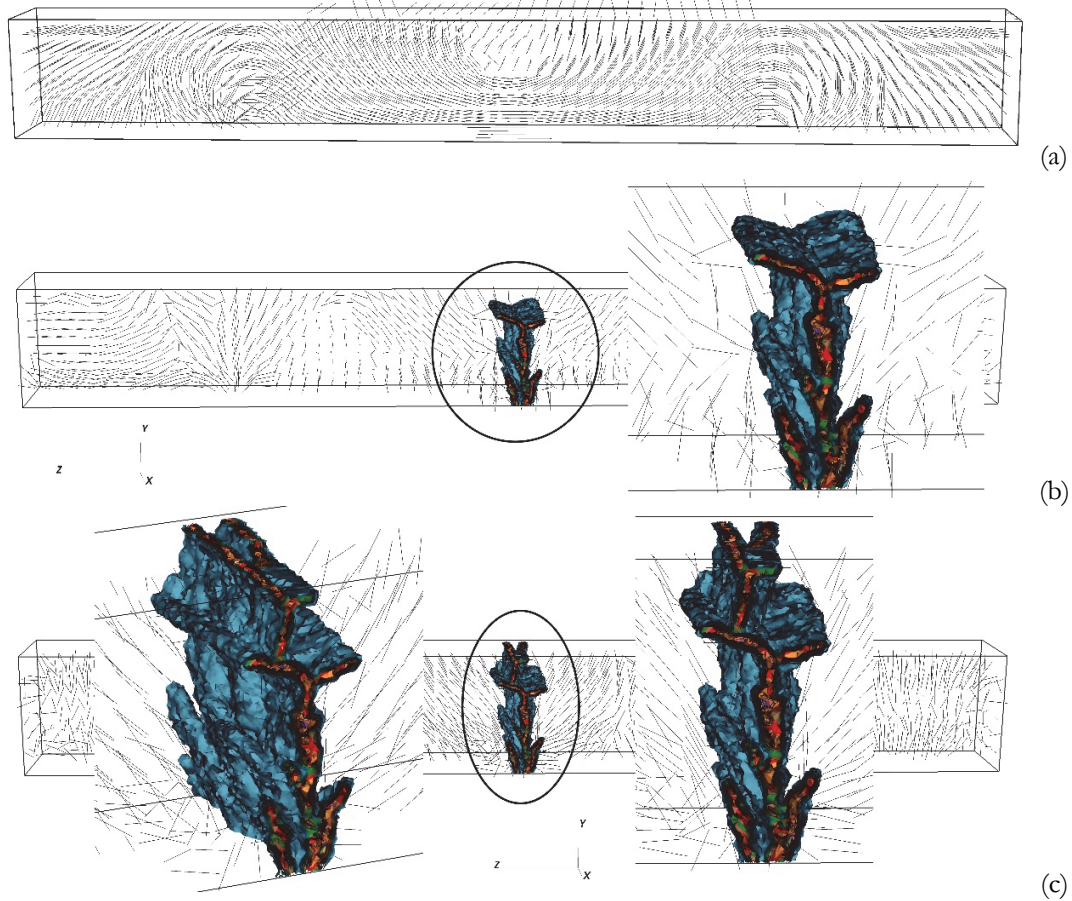

Figure 7: Stages of crack advancement and rotation of maximum principal stress axis (a-c). Patterns of the contour of inelastic strain intensity are combined with the axis orientation of the maximum principal stress.
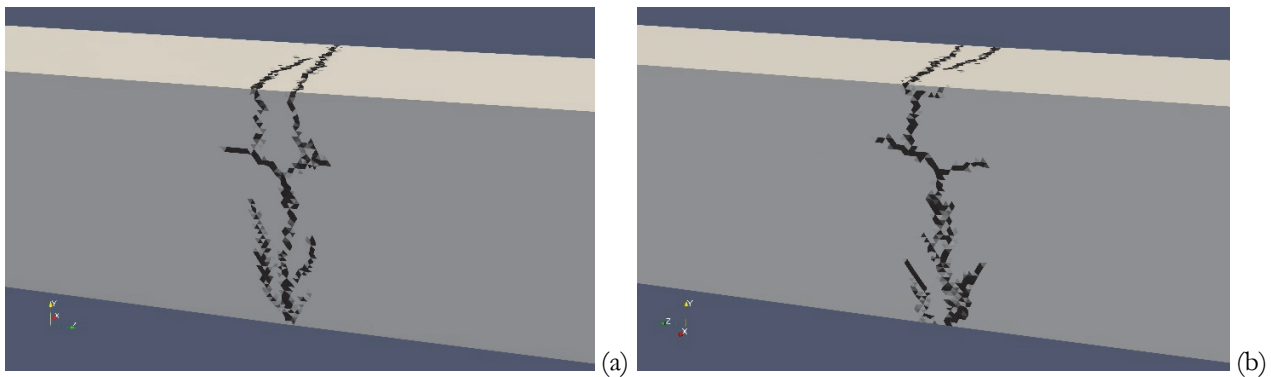

Figure 8: The final pattern of macroscopic fracture, views from two opposite sides of the specimen are illustrated.

SUMMARY

Production of advanced materials on the basis of metal oxides ceramics is booming production area. The creation of materials with necessary mechanical properties is an actual problem of materials science, which is solved on the basis of detailed experimental studies. However, the involvement of modern technologies based on CAD/CAM can significantly reduce costs when designing new materials. In this context, the creation of digital twins of materials and the formulation of fracture criteria is one of the most urgent tasks of materials science.

In this work, the FEM simulation-based approach is utilized. A digital twin of a laboratory specimen was created. Specimens were obtained by sintering powder of technically pure aluminum oxide. Microstructure studies were performed, as well as experiments on three-point bending of laboratory specimens.

Numerical simulation of the specimen's deformation and fracture at three-point bending loading was performed in a three-dimensional formulation. The inelastic deformation of the sample is described in the work by the Drucker – Prager model with the non-associated plastic flow rule; the deformation criterion which is based on the accumulated intensity of inelastic strain is selected as the fracture criterion. All parameters of the model, with the exception of the dilatancy coefficient, were validated on the basis of experimental data and correspond to the effective characteristics, which have been recently obtained from the mesoscale simulation.

Alumina ceramics demonstrate typical brittle behavior, the crack path is rather tortuous with the dominant mode I mechanism.

The results of the numerical simulation are in good agreement with the experimental study.

ACKNOWLEDGMENTS

REFERENCES

[1] Ruys, A. (2019). Processing, structure, and properties of alumina ceramics, In: Alumina ceramics: Biomedical and clinical applications, Woodhead Publishing, pp. 71–121. DOI: 10.1016/C2017-0-01189-8.

[2] Staub, D., Meille, S., Le Corre, V., Rouleau, L. and Chevalier, J. (2016). Identification of a damage criterion of a highly porous alumina ceramic, Acta Materialia, 107, pp. 261–272. DOI: 10.1016/j.actamat.2016.01.071.

[3] Savija, B., Smith, G.E., Liu, D., Schlangen, E. and Flewitt, P.E.J. (2019). Modelling of deformation and fracture for a model quasi-brittle material with controlled porosity: Synthetic versus real microstructure, Engineering Fracture Mechanics, 205, pp. 399–417. DOI: 10.1016/j.engfracmech.2018.11.008.

[4] Grigoriev, A., Shilko, E., Skripnyak, V., Smolin, A. and Psakhie, S. (2014). Multiscale numerical study of fracture and strength characteristics of zirconium alumina concrete with use of the particle-based MCA method, Procedia Materials Science, 3, pp. 936–941. DOI: 10.1016/j.mspro.2014.06.152.

[5] Mikushina, V.A. and Smolin, I.Yu. (2018). Simulation of mesoscopic fracture of ceramics with hierarchical porosity, AIP Conference Proceedings, 2053, 030041. DOI: 10.1063/1.5084402.

[6] Johnson, G. (1977). High-velocity impact calculations in three dimensions, Journal of Applied Mechanics, 44, pp. 95–100. DOI:10.1115/1.3424022

[7] Drucker, D.C. and Prager, W. (1952). Soil Mechanics and plastic analysis or limit design, Q. Applied Math., 10, pp. 157–165.

[8] Makarov, P.V., Eremin, M.O. and Kostandov, Yu.A. (2014). Prefracture time of gabbro specimens in a damage accumulation model, Physical Mesomechanics, 17, pp. 199–203. DOI: 10.1134/S1029959914030047.